Comparative study of the oxide scale thermally grown on titanium alloys by ion beam analysis techniques and scanning electron microscopy

A. Gutiérrez[a)]
Departamento de Física Aplicada, Universidad Autónoma de Madrid, Cantoblanco, E-28049 Madrid, Spain

F. Pászti
KFKI Research Institute for Particle and Nuclear Physics, H-1525 Budapest, Hungary; and Centro de Microanálisis de Materiales, Cantoblanco, E-28049 Madrid, Spain

A. Climent-Font
Departamento de Física Aplicada, Universidad Autónoma de Madrid, Cantoblanco, E-28049 Madrid, Spain; and Centro de Microanálisis de Materiales, Cantoblanco, E-28049 Madrid, Spain

J.A. Jiménez
Centro Nacional de Investigaciones Metalúrgicas, CSIC, E-28040 Madrid, Spain

M.F. López
Instituto de Ciencia de Materiales de Madrid, CSIC, Cantoblanco, E-28049 Madrid, Spain

(Received 28 September 2007; accepted 12 May 2008)

In the present work, the oxide layers developed at elevated temperature on three vanadium-free titanium alloys, of interest as implant biomaterials, were studied by Rutherford backscattering spectroscopy, elastic recoil detection analysis, and scanning electron microscopy. The chemical composition of the alloys investigated, in wt%, was Ti–7Nb–6Al, Ti–13Nb–13Zr, and Ti–15Zr–4Nb. Upon oxidation in air at 750 °C, an oxide scale forms, with a chemical composition, morphology, and thickness that depend on the alloy composition and the oxidation time. After equal exposure time, the Ti–7Nb–6Al alloy exhibited the thinnest oxide layer due to the formation of an Al_2O_3-rich layer. The oxide scale of the two TiNbZr alloys is mainly composed of Ti oxides, with small amounts of Nb and Zr dissolved. For both TiNbZr alloys, the role of the Nb-content on the mechanism of the oxide formation is discussed.

I. INTRODUCTION

Titanium and titanium alloys have been widely used in medical applications due to their excellent corrosion resistance and mechanical properties. Among all commercially available alloys, Ti–6Al–4V has been the most-used titanium alloy for artificial hip joints for many years. Despite the exceptional properties of this alloy, recent investigations report on the release of metallic ions from surgical implants, which could induce harmful effects.[1–5] The results of different studies indicate that metallic vanadium is strongly toxic to cells, and aluminium has been associated with potential neurological disorders.[6–8] Thus, much research effort is being devoted to develop vanadium-free alloys with improved biocompatibility and similar corrosion resistance and mechanical properties to Ti–6Al–4V alloy.[9–15]

The biocompatibility of metallic biomaterials is related to their corrosion resistance in biological systems. The excellent corrosion behavior of titanium-based alloys in aggressive environments is achieved due to the formation of a stable, tightly adherent, passive layer.[16–19] This layer is nothing but the surface oxide film generated spontaneously by reaction with oxygen from the atmosphere. A possible approach to improving the corrosion resistance of titanium alloys would be to increase the thickness of the outer oxide layer. This can be easily and economically attained by subjecting the titanium alloys to an oxidation treatment at elevated temperature.

In previous works, three Ti alloys without V, of composition (in wt%) Ti–7Nb–6Al, Ti–13Nb–13Zr, and Ti–15Zr–4Nb, were selected as potential biomaterials, and a thick oxide coating was developed on their surface by thermal oxidation.[20,21] Several properties of these alloys, including corrosion behavior, surface topography, and

---

[a)] Address all correspondence to this author.
e-mail: a.gutierrez@uam.es
DOI: 10.1557/JMR.2008.0281

© 2008 Materials Research Society

microstructure, were investigated both before and after the oxide layer was grown.[20–24] The chemical composition of the outermost layers is of particular importance to evaluate a biomaterial, since these surface layers will be in direct contact with biological tissues. Consequently, surface chemical analysis was also performed on the Ti alloys, both with and without thermal treatment, by x-ray photoelectron spectroscopy (XPS) and x-ray absorption spectroscopy (XAS).[25–27] XPS is a surface-sensitive technique, which provides information on the chemical composition of the last atomic layers (~10–20 Å). On the other hand, the sampling depth of XAS, which reaches in total electron yield mode of 70–100 Å, gives complementary information for deeper surface layers.

Although the outermost surface is certainly a critical factor in the evaluation of new biomaterials, the determination of the complete in-depth chemical composition of the oxide scale is also important. This composition will influence the diffusion of ionic species toward the surface and hence the toxicity and biocompatibility of the material.[28,29] The goal of the present investigation is to use spectroscopic techniques with larger sampling depth than XPS and XAS to analyze the in-depth chemical composition of the oxide scale with the aim of understanding activity of the different alloying elements during thermal oxidation. Thus, we have performed a thermal treatment on three V-free titanium alloys: Ti–6Al–7Nb, Ti–13Nb–13Zr, and Ti–15Zr–4Nb. Subsequently, their oxide scales were studied by Rutherford backscattering spectroscopy (RBS), elastic recoil detection analysis (ERDA), and scanning electron microscopy (SEM).

II. EXPERIMENTAL

Three Ti-based alloys of composition (in wt%) Ti–7Nb–6Al, Ti–13Nb–13Zr, and Ti–15Zr–4Nb were prepared by arc melting and then casting in a copper coquille under high vacuum. The specimens were cut from as-cast ingots by electrospark-erosion. Before the oxidation process, the sample surfaces were abraded and polished using diamond pastes with successively smaller particle size. In the final stage of this process, colloidal silica was used to ensure a surface free of mechanical deformation. After polishing, the specimens were ultrasonically cleaned with acetone before oxidation. The material in this state is labeled as the "as-received" sample. At this point, some specimens were isothermally oxidized in air in a tube furnace at 750 °C for exposition times of 90 min, 6 h, and 24 h.

The surface composition of the outer layers of the as-received and oxidized samples was characterized using two ion beam analysis techniques, RBS and ERDA. Additionally, the microstructure of the oxide layers was investigated by means of SEM equipped with energy dispersive x-ray microanalysis (EDX). Metallographic preparation included mounting the samples in bakelite and polishing by the conventional method. For the cross-sectional views, the surface of the oxidized samples was previously coated with a mixed layer, composed of a thin sputtered gold layer and a thicker electrolytically deposited copper layer, to avoid scale loss during metallographic preparation.

RBS and ERDA experiments were performed using the 5 MeV tandem accelerator of the Centro de Microanálisis de Materiales (CMAM), at the Universidad Autónoma de Madrid.[30] For the RBS technique, the energies of the analyzing He^+ ions were 2, 3.035, and 5.61 MeV, respectively. At greatest energy level, the analyzed depth reached 4×10^{19} atoms/cm^2, and the sensitivity for oxygen and carbon increased two orders of magnitude. ERDA experiments were also carried out using 28 MeV Si^{5+} ions. Finally, the RBS and ERDA spectra were fitted using the RBX code.[31]

III. RESULTS AND DISCUSSION

Figure 1 shows top views of the surface of Ti–7Nb–6Al, Ti–13Nb–13Zr, and Ti–15Zr–4Nb after thermal treatment at 750 °C for 24 h. As can be observed, the surface morphologies are different for the three samples. This diversity is mainly related to the different bulk chemical compositions of the alloys, which not only lead to different oxide layer compositions, but also to α and β phase distributions.[25–27] After oxidation, the surface of Ti–6Al–7Nb alloy presents an anisotropic corrugated structure with well-defined groove borders between regions, as observed in the SEM image of Fig. 1(a). This structure looks similar to the lamellar (α–β) bulk microstructure observed for the as-received sample[22] and differs from the granular structure along randomly oriented lines shown in Fig. 1(b) for Ti–13Nb–13Zr. Finally, the Ti–15Zr–4Nb alloy exhibits a locally homogeneous surface, with a polygonal microstructure of prevailing hexagonal shape [Fig. 1(c)].

Figure 2 shows cross-sectional views of the Ti–7Nb–6Al, Ti–13Nb–13Zr, and Ti–15Zr–4Nb alloys oxidized for 24 h at 750 °C. These SEM micrographs show clear differences in the thickness and compaction of the oxide scales formed on the three alloys. The Ti–7Nb–6Al alloy developed a thin, compact, and homogeneous scale about 2 μm thick, whereas the TiNbZr alloys present a much looser and thicker scale, around 10 and 25 μm thick for Ti–13Nb–13Zr and Ti–15Zr–4Nb, respectively. Additionally, both TiNbZr alloys clearly show pores and longitudinal fissures at the metal–oxide interface.

Although rutile is a protective coating at room temperature, its behavior dramatically changes at temperatures above 500 °C. At this temperature, a rutile scale becomes permeable to inward oxygen diffusion, favoring

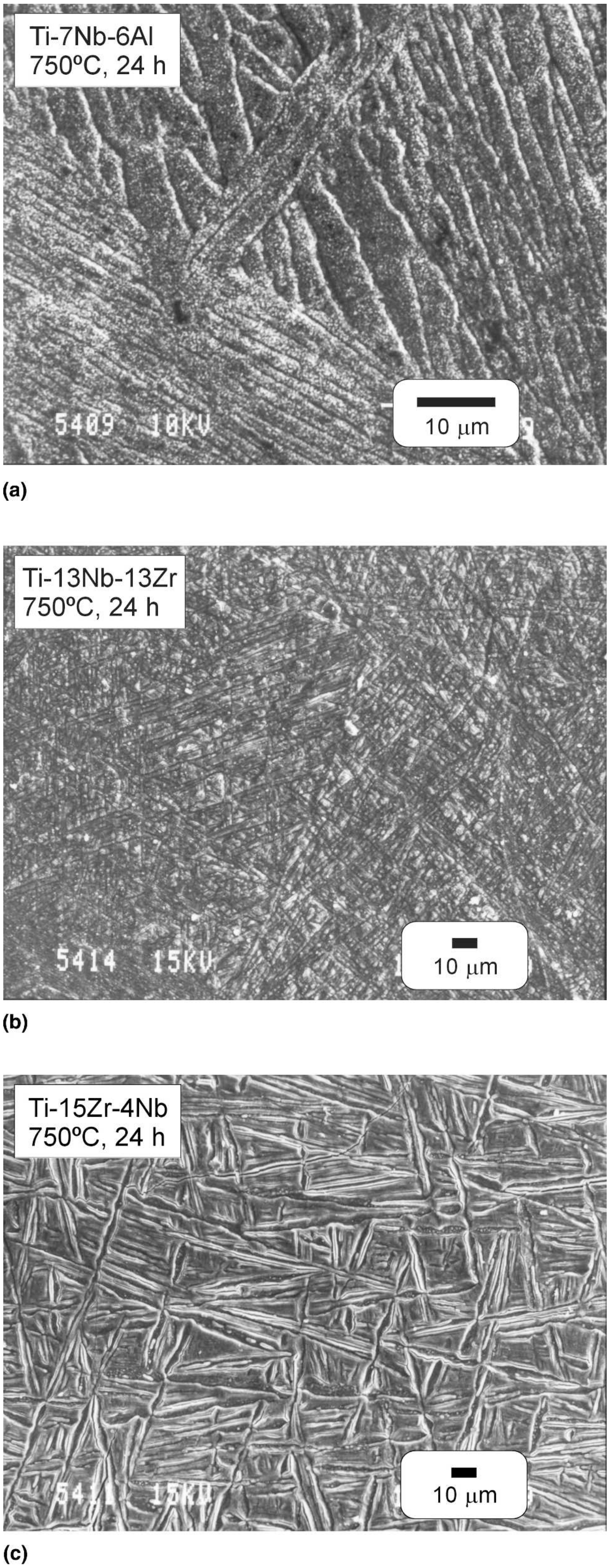

FIG. 1. Top-view SEM micrographs of Ti–7Nb–6Al, Ti–13Nb–13Zr, and Ti–15Zr–4Nb alloys after heat treatment performed at 750 °C in air for 24 h.

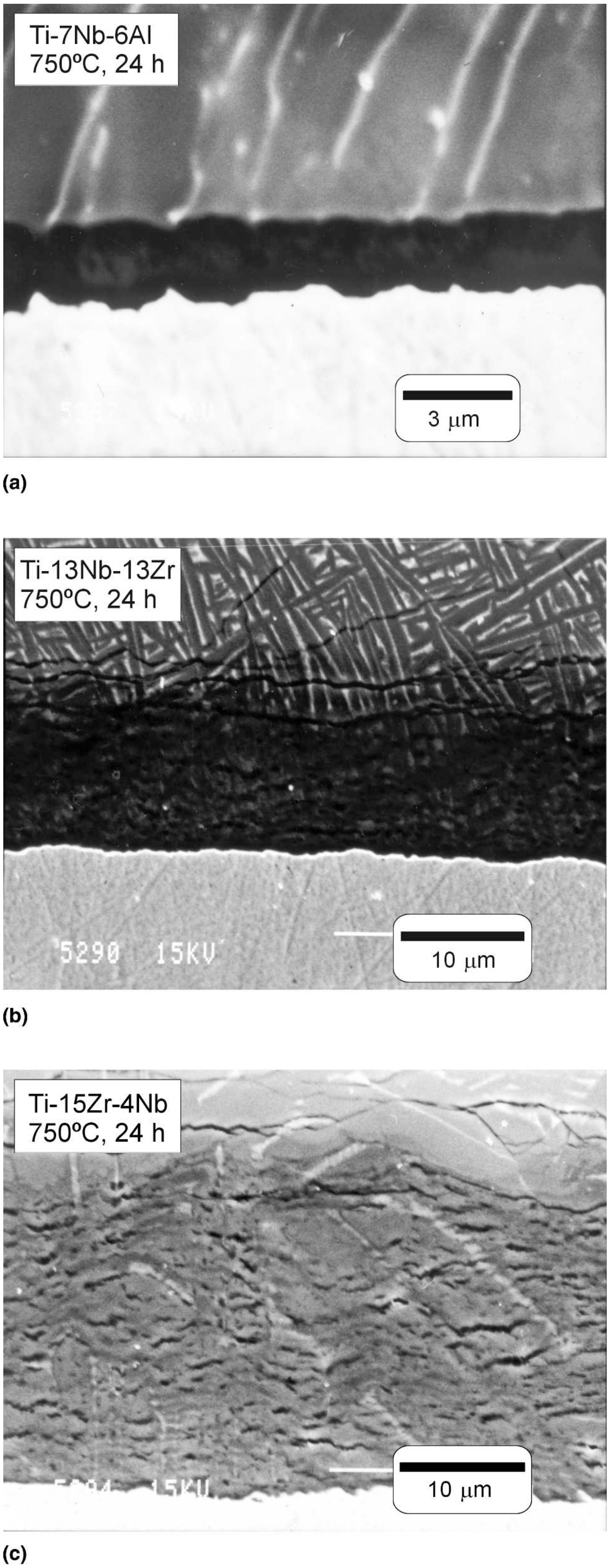

FIG. 2. Cross-sectional SEM micrographs of the oxide layer formed after heat treatment at 750 °C for 24 h in air on Ti–7Nb–6Al, Ti–13Nb–13Zr, and Ti–15Zr–4Nb.

the further oxidation of the alloy. It is well known that the addition of Al notably improves the oxidation resistance of Ti due to the growth of an outer Al_2O_3-rich layer.[32–34] This layer retards the growth of the oxide scale considerably, since it hinders inward oxygen diffusion. This effect can even be enhanced by the presence of other elements like Nb.[35] According to previous x-ray diffraction (XRD) data, the oxide scale of Ti–7Nb–6Al alloy is composed of TiO_2 in rutile form and alpha-alumina, while the oxide scales of the two oxidized TiNbZr alloys are mainly composed of TiO_2 in the rutile form.[20] In these XRD measurements, Nb and Zr oxides were not detected due to their dissolution in the TiO_2 and/or Al_2O_3 lattice forming solid solutions.

To understand the mechanisms of oxide formation, thermodynamic properties must be taken into account. The curves of the standard free energies of formation of oxides versus temperature, i.e., the well-known Ellingham/Richardson diagrams,[36] show that Ti and Zr oxidation are thermodynamically less favored than Al or Nb oxidation. The high activity of Al during oxidation of the Ti–7Nb–6Al alloy leads to the formation of the alumina-rich scale observed on this sample. However, after oxidation, the two TiNbZr alloys show a scale composed mainly of TiO_2, counter to the thermodynamic expectation. This can be explained considering that the activity of different alloying elements during oxidation is a function of both the concentration of these elements and the element diffusion tendency along the oxide layer. In both TiNbZr alloys, during the first stages of the oxidation process, the huge Ti content leads to the initial formation of a TiO_2 outer layer. After this first period of the thermal process, the oxidation rate is mainly controlled by ion diffusion through the oxide scale. Because Nb and Zr oxides were hardly detected by XRD, Ti diffusion inside this oxide layer seems to be favored, promoting a continuous growth of the TiO_2 layer as the oxidation time is increased.

As mentioned, the oxide layer thickness of both TiNbZr alloys after the 24-h thermal treatment is much larger than that of the oxidized Ti–7Nb–6Al alloy. To compare samples with similar oxide layer thickness, the oxidation time for the TiNbZr alloys was diminished to 6 h. As can be seen in Fig. 3, the oxide layer thickness of both alloys is considerably lower than that obtained after 24 h oxidation and closer to that of the Ti–7Nb–6Al shown in Fig. 2. In the case of the Ti–13Nb–13Zr alloy oxidized for 6 h, the scale is more uniform than that for longer times, with no longitudinal fissures and with a thickness of ~3–4 μm. On the other hand, for the same oxidation time, the Ti–15Zr–4Nb alloy already shows a rather inhomogeneous layer with uneven thickness values, which exceeds 10 μm in some points. In this case, some fissures are visible along the sample, parallel to the metal/oxide interface. Since the main difference between both alloys is the Nb-content, the lower oxidation kinetics of the Ti–13Nb–13Zr alloy was associated with its higher Nb content. This result is in agreement with previous works, which report a considerabe improvement of the Ti oxidation resistance by addition of Nb.[37,38]

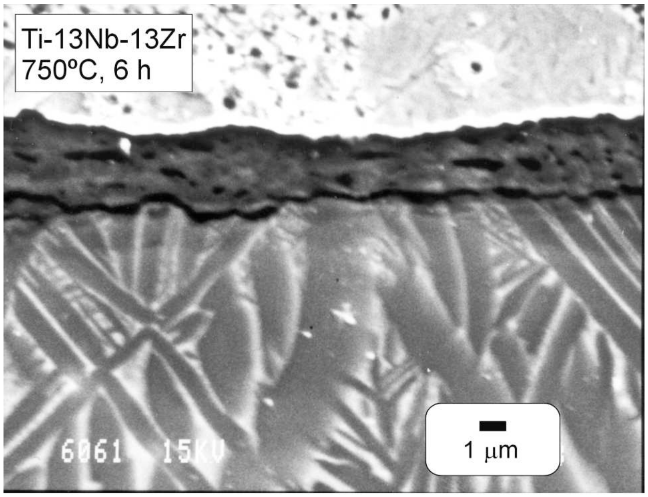

(a)

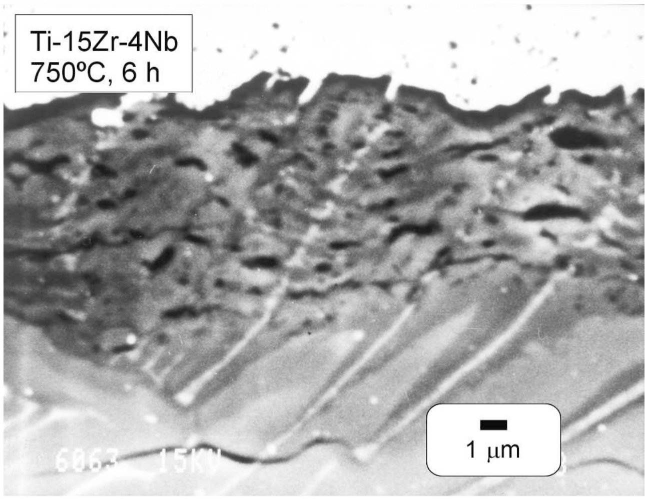

(b)

FIG. 3. Cross-sectional SEM micrographs of the oxide layer formed after heat treatment at 750 °C for 6 h in air on (a) Ti–13Nb–13Zr and (b) Ti–15Zr–4Nb.

To gain further insight into the mechanisms and kinetics of the oxide scale formation, it is essential to know the in-depth composition profile along the oxide layer. RBS and ERDA are suitable techniques because they are not destructive and their depth sensitivity is on the order of the oxide thickness. As mentioned in the experimental details, each sample was measured with RBS at three different ion energies and also with ERDA. The experimental data were then fitted, assuming that the in-depth composition varies smoothly, and the various elemental fractions were represented by error-function type curves. The composition profiles were then optimized to find the best fit for all four experimental spectra. Figure 4 shows, as an example, the result of the fit for the 3.035 MeV RBS spectrum of the Ti–7Nb–6Al alloy oxidized at 750 °C for 90 min. The points correspond to the experimental RBS data while the solid line through the data points represents the results of the fitting procedure using the RBX code. This analysis was carried out simultaneously for the different ion beam spectra, so the three different RBS signals measured with He^+ ions of 2, 3.035, and 5.61 MeV, respectively, combined with the ERDA data obtained using 28 MeV Si^{5+} ions, were involved at the same time in the fitting procedure. Thus, the best experiment–theory fit result gives rise to a particular element concentration depth profile. This method was applied for all samples studied both as-received and thermally oxidized, generating the element concentration depth profiles for each specimen.

Figure 5 exhibits the elemental depth profile for as-received and oxidized Ti–7Nb–6Al alloys as a result of the fitting procedure described above. For all samples, the same curve assignment is used. Thus, the solid, dashed, dotted, and dash-dotted lines correspond to Ti, O, Al, and Nb depth profiles, respectively. The conversion from atoms per square centimeter to a length scale in microns was accomplished by assuming an ideal mixing of the most stable compounds for the elemental profile at each depth value and by using a standard density value for each of these compounds. We estimate the error in the depth values to be within a 10% of the real values. In the case of the as-received sample, since the passive layer formed spontaneously in contact with air is only on the order of several nanometers, the signal obtained for the different elements remains constant throughout the depth of the material. In this case, the values exhibited are close to the chemical composition of the alloy, as can be seen in Table I. In Table I, the atomic percentage composition is shown for the as-received alloys as derived from the sample preparation (named "nominal bulk concentration"), the as-received alloys as deduced from the ion beam analysis techniques (labeled as "bulk concentration"), and the surface of the 24 h oxidized samples (called "full oxidized, surface concentration"), as the most external elemental composition values obtained from the RBS analysis, i.e., the values shown in Figs. 5–7 for 0-μm depth for the 24-h oxidized samples.

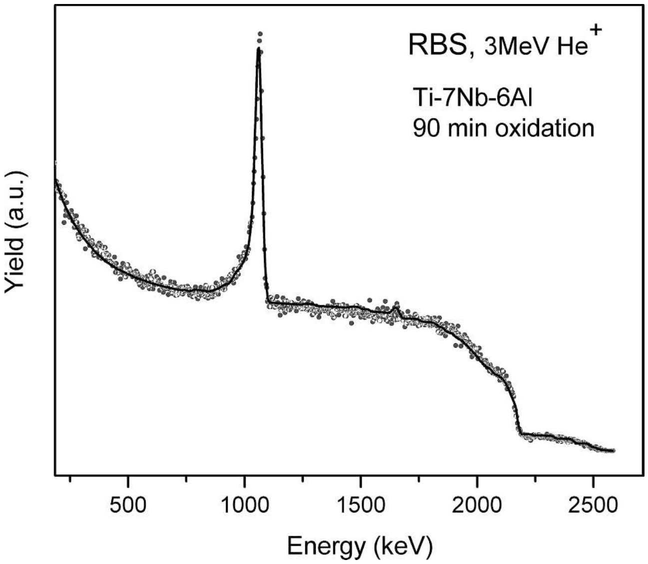

FIG. 4. RBS spectrum obtained with 3.035 MeV He^+ ions on the Ti–7Nb–6Al alloy oxidized at 750 °C for 90 min. The solid line through the data points represents the result of the fitting procedure performed simultaneously on this spectrum and those obtained by three complementary ion beam techniques on the same sample (see text).

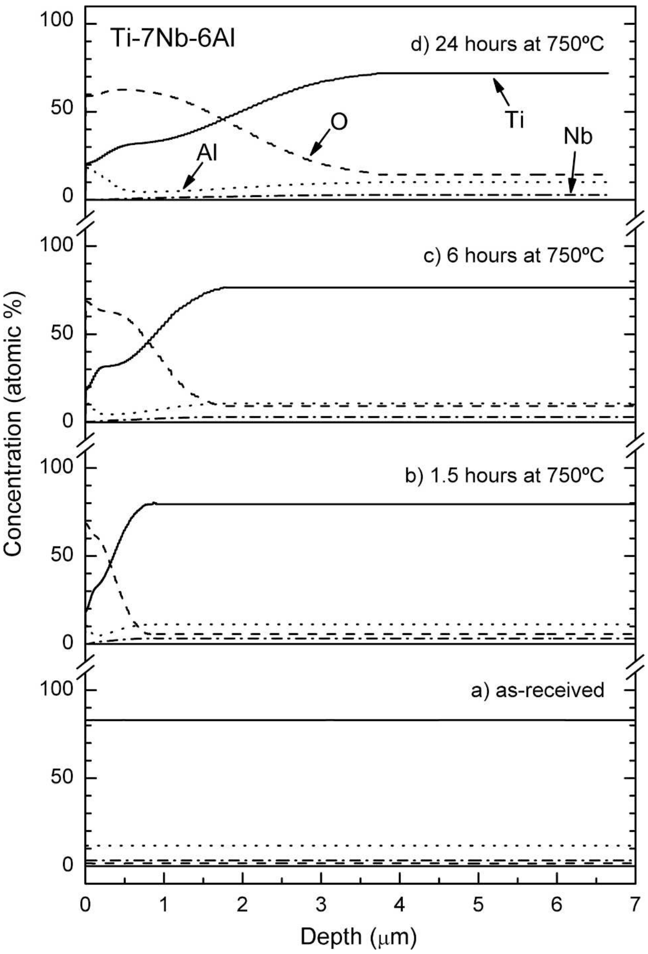

FIG. 5. Element concentration depth profiles obtained from RBS and ERDA for the as-received and oxidized Ti–7Nb–6Al alloys.

The depth profiles obtained for the heat-treated samples in Fig. 5 clearly show the gradual formation of an oxide layer, which becomes thicker in a continuous way as a function of the oxidation time until it a maximum value for 24 h. We have selected, as an estimate for the oxide layer thickness, the depth at which the oxygen decreasing curve meets the Ti rising curve, which, in the

TABLE I. Elemental concentration values for the three Ti-alloys: bulk nominal composition, bulk composition of the as-received specimens as determined by RBS-ERDA, and surface composition of the samples oxidized at 750 °C for 24 h, as obtained from the outermost concentration given by RBS-ERDA.

	O	Ti	Al	Nb
Ti–7Nb–6Al				
Nominal bulk concentration (at.%)	· · ·	86.0	10.4	3.6
Bulk concentration (at.%)	1.7	83.4	11.6	3.3
Full oxidized, surface concentration (at.%)	60.4	18.6	21.0	0
Ti–13Nb–13Zr				
Nominal bulk concentration (at.%)	· · ·	84.5	7.8	7.7
Bulk concentration (at.%)	1.7	83.9	7.2	7.2
Full oxidized, surface concentration (at.%)	67.9	30.7	0	1.4
Ti–15Zr–4Nb				
Nominal bulk concentration (at.%)	· · ·	90.0	8.7	1.3
Bulk concentration (at.%)	3.4	86.2	8.2	2.2
Full oxidized, surface concentration (at.%)	70.1	29.2	0	0.7

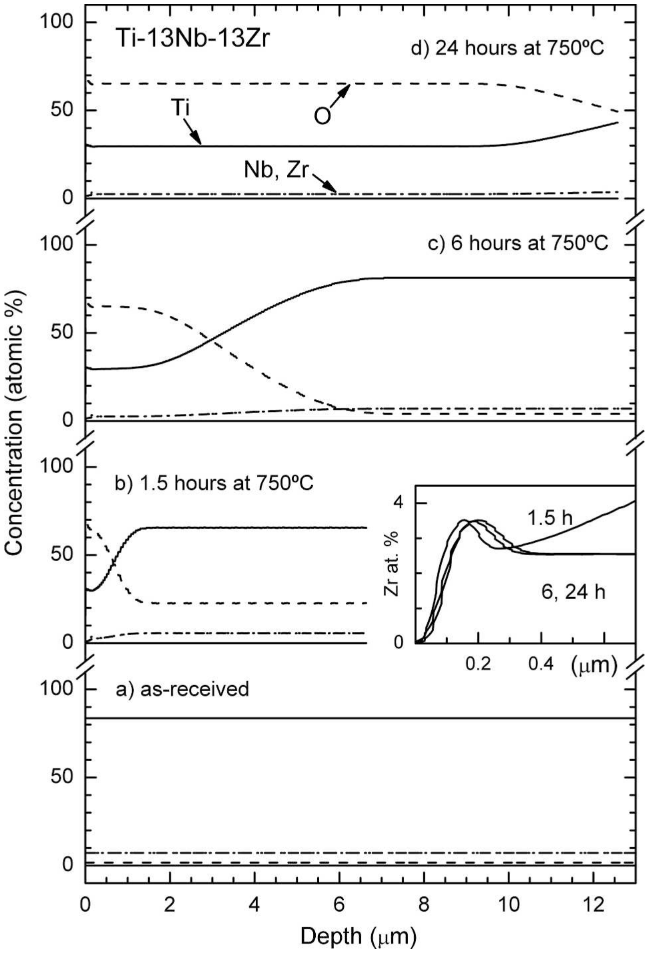

FIG. 6. Element concentration depth profiles obtained from RBS and ERDA for the as-received and oxidized Ti–13Nb–13Zr alloys.

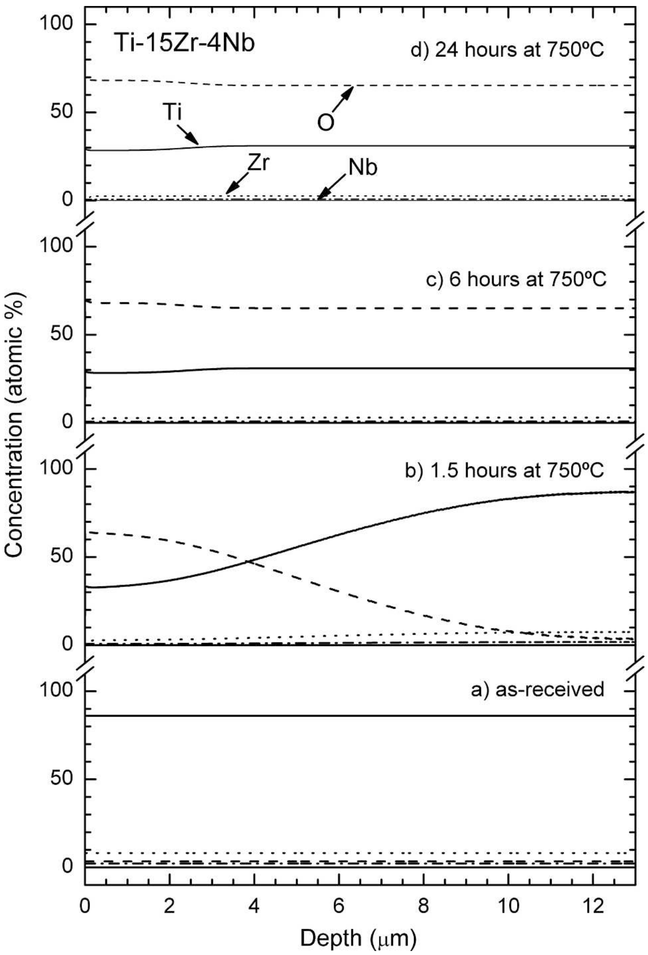

FIG. 7. Element concentration depth profiles obtained from RBS and ERDA for the as-received and oxidized Ti–15Zr–4Nb alloys.

case of the Ti–7Nb–6Al alloy oxidized at 750 °C for 24 h, has an approximate value of 1.8 μm, in agreement with the value observed in the SEM image of Fig. 2. Regarding the evolution of the elemental concentration curves, all samples present a higher Al content near the surface, gradually decreasing with depth to a minimum value, to increase again to approximately the bulk concentration. The concentration of Al near the surface is about twice the bulk composition for the sample oxidized for 24 h. As both the thickness of the Al rich layer and the Al content near the surface increase with oxidation time, it can be concluded that Al diffuses toward the surface. Therefore, the thermal oxidation induces the formation of a surface alumina rich layer, which decreases the inward diffusion of oxygen, improving the oxidation resistance of the Ti–7Nb–6Al alloy. Figure 5 also shows an inner Al depleted layer, similar to that observed in other Al-containing alloys after thermal oxidation.[39,40] The depth at which the Al content is minimum in this depletion zone increases with oxidation time, with approximate values of 0.2, 0.3, and 0.6 μm for 1.5, 6, and 24 h, respectively. Also the thickness of the depletion zone increases with oxidation time, with approximate values of 0.5, 1, and more than 2 μm for 1.5, 6, and 24 h, respectively. The increase of the depletion zone thickness and the depth of the minimum Al concentration with oxidation time is the consequence of Al diffusion to the surface during oxidation.

It is also worth mentioning the behavior exhibited by niobium. In the as-received material, this element is present in a rather low concentration, keeping a constant value as a function of the alloy depth similar to the nominal Nb atomic percentage of the alloy. For the oxidized specimens, however, although the values at deeper levels are similar to that of the as-received sample, the outermost region of the oxide layers clearly shows Nb depletion. The Nb content grows up gradually from zero as a function of depth until it reaches the bulk value at the end of the oxide layer, similar to the results found in previous works on other alloys.[38] In a previous work by XPS on the Ti–7Nb–6Al alloy oxidized at 750 °C for 24 h, it was unexpectedly found that Nb was not present at the surface, i.e., the Nb 3*d* XPS signal was negligible.[27] The present results obtained by means of ion beam analysis techniques support this experimental evidence, giving an evolution of the Nb concentration as a function of depth due to their extreme sampling depth. As mentioned above, Nb addition has been shown to improve the oxidation resistance of Ti alloys.[35,37,38] Although the mechanisms to explain this improvement are not yet clear, Nb as substitutional cation in the rutile lattice seems to reduce the diffusion rate of oxygen-ion vacancies.[37] As this protective mechanism for Nb is not associated with the formation of Nb oxides, it would be compatible with a slight increase of Nb concentration through the scale, as observed in Fig. 5.

An interesting point revealed in Fig. 5 is the extent of the oxygen inward diffusion. Even the as-received sample shows a non-negligible, constant O-content in the whole analyzed depth, as is shown in Table I. The oxidized Ti–7Nb–6Al alloys show oxygen enrichment at the surface, which is larger for longer oxidation times, as is obviously expected. Additionally, the amount of bulk diffused oxygen, below the oxide scale, also increases with oxidation time. Such an increase in oxygen dissolution with oxidation time and temperature has also been observed in previous work.[37]

Figure 6 shows the elemental depth profiles for the as-received and oxidized Ti–13Nb–13Zr alloy. In this case, the solid, dashed, dotted, and dash-dotted lines correspond to Ti, O, Zr, and Nb, respectively. Again, the as-received sample (bottom curve) exhibits concentration values, which are in accordance with the nominal composition percentages of the alloy (see Table I). Due to the similar atomic concentration of Nb and Zr (13% in weight in both cases and close atomic number), the Nb line is almost indistinguishable from Zr in all curves shown in Fig. 6. For the oxidized samples, the surface Nb contribution is rather low but not zero (see value for 24 h oxidation in Table I), in contrast to the oxidized Ti–7Nb–6Al case. This result is again in agreement with previous XPS results on this alloy, where a low but non-zero Nb emission could be detected at the surface.[27] As can be observed in Fig. 6 for all oxidized samples, the low initial Nb concentration grows up slowly with depth until the bulk value is reached. In contrast to Nb, the Zr surface concentration is zero in all cases (see Table I), but just below the outermost surface, a small peak is observed [see, e.g., the inset in Fig. 6(c)], which at some point even surpasses the Nb concentration. This small intensity enhancement abruptly drops to the Nb values for a sample depth of ~0.25 μm. This result reveals the existence of a Zr segregation zone at an intermediate layer just underneath the oxidized alloy surface. On the other hand, the surface Zr concentration, which is lower than the Nb one, is again in agreement with previous XPS results, where the Zr emission at the surface is lower than the Nb signal.[27] It is important to emphasize that although the results show a good correlation, the different sampling depths of RBS and XPS provide information of different surface regions.

For the Ti–13Nb–13Zr alloy, the oxide layer is composed mainly of Ti oxide, since neither Nb nor Zr oxides are present in the XRD pattern. This result suggests that although Nb oxidation should be thermodynamically promoted, the high amount of Ti in the alloy causes the formation of an oxide layer mainly composed of Ti. As the amount of Nb and Zr near the surface is lower than the bulk composition, it was concluded that diffusion of these elements through the scale is rather low. At the surface of the oxidized samples, only small amounts of Nb and no Zr were observed, revealing that Nb oxidation is favored against Zr. This result agrees with the Ellingham/Richardson diagrams, which show that Nb oxidation is more thermodynamically favored than Zr oxidation. However, the observation of Zr segregation at an intermediate layer suggests that Zr diffusion inside the oxide layer is also not negligible.

For all oxidized samples shown in Fig. 6, the Ti and O surface concentration values are similar, independent of oxidation times. This is in agreement with previous XAS results, where in all cases, formation of a TiO_2 surface layer was observed.[26] The thickness of the oxide layer becomes larger for longer oxidation exposures. Thus, the 6-h oxidized Ti–13Nb–13Zr alloy shows a thickness of ~3 μm, which is in agreement with the SEM observations shown in Fig. 3. Finally, the oxide scale thickness for the 24-h heated sample has a value of approximately 13 μm, as can be deduced from Fig. 6, which again nicely agrees with the micrograph shown in Fig. 2.

The elemental depth profiles of the as-received and oxidized Ti–15Zr–4Nb alloys are represented in Fig. 7. Again, the same assignment as in the previous case is used, with the solid, dashed, dotted, and dash-dotted lines corresponding to Ti, O, Zr, and Nb profiles, respectively. The as-received curves indicate concentration values that resemble those of the base alloy, as can be also seen in Table I. This alloy is rather similar to Ti–13Nb–13Zr in the sense that it has the same alloying elements. However, the relative concentration is different, and this has major implications. Thus, Ti–15Zr–4Nb has a lower β-phase/α-phase ratio due to a lower relative amount of the β-stabilizer niobium. Among others, this lower Nb-content is responsible for a different oxidation kinetics, which leads to a thicker oxide layer for Ti–15Zr–4Nb than it does for Ti–13Nb–13Zr, as discussed above and observed in the SEM cross-sectional views of Figs. 2 and 3. Accordingly, the data exhibited in Fig. 7 indicate a thicker oxide layer for the oxidized Ti–15Zr–4Nb alloy. For an oxidation time of 1.5 h, the oxide layer is ~4 μm thick, and for 6 h it is already thicker than 13 μm. This result is just within the error limit of the SEM observation, since for the 6 h oxidized Ti–15Zr–4Nb alloy, the cross-sectional view reveals an oxide layer thickness to some extent larger than 10 μm. However, as mentioned before, this oxidized layer is inhomogeneous, showing fluctuating thickness values, which range from 10 to ~15 μm. Another difference with the Ti–13Nb–13Zr is the absence of a Zr-rich zone underneath the surface region, although in both cases the surface Zr content is zero. Again, this effect could be related to a lower amount of Nb in this alloy. As already stated, in TiNbZr alloys, the oxidation is more favored for Nb than for Zr, and Nb diffusion along the oxide layer seems to be promoted. However, the lower Nb-content in the case of Ti–15Zr–4Nb as compared to that of Ti–13Nb–13Zr leads to a lower surface Nb concentration. Thus, for the 24-h-oxidized Ti–15Zr–4Nb sample, the surface Nb contribution is not zero, in accordance with previous XPS results,[27] although it is lower than in the case of the oxidized Ti–13Nb–13Zr alloys.

IV. CONCLUSIONS

The oxide layer formed during oxidation at 750 °C on three vanadium-free titanium alloys of composition Ti–7Nb–6Al, Ti–13Nb–13Zr, and Ti–15Zr–4Nb was studied by SEM, ERDA, and RBS. The combination of SEM and ion beam analysis techniques, (ERDA and RBS) was used to study and interpret the effects of the different alloying elements on the oxidation behavior.

Concerning the oxide layer thickness, excellent agreement between SEM observations and RBS-ERDA results was found. The lowest thickness was observed on the oxidized Ti–7Nb–6Al alloys, where the formation of an outer Al_2O_3-rich layer greatly retards the growth of the oxide scale. The two TiNbZr oxidized alloys exhibit much thicker scales, mainly composed of Ti oxides, which are less homogeneous and can exhibit some fissures at the oxide layer/alloy interface.

All as-received alloys show elemental concentration values in accordance with the nominal values. After oxidation, the evolution of the different element depth profiles was related with both thermodynamic properties and diffusion ability. For Ti–7Nb–6Al oxidized alloy, surface Al segregation is clearly observed for all oxidation times, followed by an Al depletion region. It was concluded that, as both the size of the Al-rich layer and the Al content near the surface increase with oxidation time, Al diffuses toward the surface. On the other hand, the Nb concentration increases as the material depth increases from zero at the surface to the bulk value.

For both TiNbZr alloys, some Nb contribution but no Zr was measured near the surface. The presence of Nb at the surface of the oxide scale agrees with the thermodynamic expectation of preferential Nb oxidation against that of Zr. Zr diffusion seems to be less favored than Nb diffusion during the thermal processes; however, the different Nb-content in both TiNbZr alloys affects substantially their oxidation mechanisms. Nb as substitutional cation in the rutile lattice seems to reduce the diffusion rate of oxygen-ion vacancies, improving the oxidation resistance.

ACKNOWLEDGMENTS

The authors gratefully acknowledge Prof. G. Fommeyer from Max Planck Institut für Eisenforschung (Düsseldorf, Germany) for kindly supplying the Ti alloy specimens. This work has been supported by Project Nos. 07N-0050-1999 and 07N-0066-2002 of the Spanish “Programa de Tecnología de los Materiales de la Comunidad Autónoma de Madrid,” by the “Nanoselect” project of the Spanish Consolider-Ingenio 2007 program, by Project No. MAT2007-66719-C03-03 of the Spanish “Ministerio de Educación y Ciencia,” and by the Hungarian OTKA Grant No. T-046238. F.P. acknowledges the Spanish *Ministerio* de Educación, Cultura y Deporte for financial support through a Sabbatical Year Grant (No. SAB2000-0243).

REFERENCES

1. B.W. Callen, B.F. Lowenberg, S. Lugowski, R.N.S. Sodhi, and J.E. Davies: Nitric-acid passivation of Ti6Al4V reduces thickness of surface oxide layer and increases trace-element release. *J. Biomed. Mater. Res.* **29,** 279 (1995).
2. A. Sargeant and T. Goswami: Hip implants—Paper VI—Ion concentrations. *Mater. Des.* **28,** 155 (2007).
3. J.J. Jacobs, A.K. Skipor, J. Black, R.M. Urban, and J.O. Galante: Release and excretion of metal in patients who have a total hip-replacement component made of titanium-base alloy. *J. Bone Joint Surg.* **73-A,** 1475 (1991).
4. S.G. Steinemann: Corrosion of surgical implant—In vivo and in vitro test, in *Evaluation of Biomaterials*, edited by G.D. Winter, J.L. Leray, and K. de Groot (Wiley, New York, 1980), pp. 1–34.
5. P.D. Bianco, P. Ducheyne, and J.M. Cuckler: Local accumulation

of titanium released from a titanium implant in the absence of wear. *J. Biomed. Mater. Res.* **31,** 227 (1996).

6. P.G. Laing, A.B. Ferguson, Jr., and E.S. Hodge: Tissue reaction in rabbit muscle exposed to metallic implants. *J. Biomed. Mater. Res.* **1,** 135 (1967).
7. D.P. Perl and A.R. Brody: Alzheimer's disease: X-ray spectrometric evidence of aluminium accumulation in neurofibrillary tangle-bearing neurons. *Science* **208,** 297 (1980).
8. J. Black: Does corrosion matter? *J. Bone Joint Surg.* **70-B,** 517 (1988).
9. Y. Okazaki, S. Rao, Y. Ito, and T. Tateishi: Corrosion resistance, mechanical properties, corrosion fatigue strength and cytocompatibility of new Ti alloys without Al and V. *Biomaterials* **19,** 1197 (1998).
10. N.T.C. Oliveira, E.A. Ferreira, L.T. Duarte, S.R. Biaggio, R.C. Rocha-Filho, and N. Bocchi: Corrosion resistance of anodic oxides on the Ti–50Zr and Ti–13Nb–13Zr alloys. *Electrochim. Acta* **51,** 2068 (2006).
11. Y.L. Hao, S.J. Li, S.Y. Sun, C.Y. Zheng, and R. Yang: Elastic deformation behavior of Ti–24Nb–4Zr–7.9Sn for biomedical applications. *Acta Biomater* **3,** 277 (2007).
12. W.F. Ho, C.P. Ju, and J.H. Chern Lin: Structure and properties of cast binary Ti–Mo alloys. *Biomaterials* **20,** 2115 (1999).
13. L. Trentani, F. Pelillo, F.C. Pavesi, L. Ceciliani, G. Cetta, and A. Forlino: Evaluation of the TiMo12Zr6Fe2 alloy for orthopaedic implants: In vitro biocompatibility study by using primary human fibroblasts and osteoblasts. *Biomaterials* **23,** 2863 (2002).
14. K. Maehara, K. Doi, T. Matsushita, and Y. Sasaki: Application of vanadium-free titanium alloys to artificial hip joints. *Mater. Trans.* **43,** 2936 (2002).
15. X.T. Zu, X.D. Feng, Z.G. Wang, G.T. Zeng, L.B. Lin, Y.L. Li, and X.Q. Huang: Characterisation of the oxide scale on a Ti–2Al–2.5Zr alloy with and without pre-oxidation in an alkaline steam at 300 degrees C. *Surf. Coat. Technol.* **148,** 216 (2001).
16. I. Dugdale and J.B. Cotton: The anodic polarization of titanium in halide solutions. *Corros. Sci.* **4,** 397 (1964).
17. J. Pan, D. Thierry, and C. Leygraf: Electrochemical impedance spectroscopy study of the passive oxide film on titanium for implant application. *Electrochim. Acta* **41,** 1143 (1996).
18. J.E.G. Gonzalez and J.C. Mirza-Rosca: Study of the corrosion behavior of titanium and some of its alloys for biomedical and dental implant applications. *J. Electroanal. Chem.* **471,** 109 (1999).
19. S. Tamiselvi, V. Raman, and N. Rajendran: Corrosion behavior of Ti–6Al–7Nb and Ti–6Al–4V ELI alloys in the simulated body fluid solution by electrochemical impedance spectroscopy. *Electrochim. Acta* **52,** 839 (2006).
20. M.F. López, J.A. Jiménez, and A. Gutiérrez: Corrosion study of surface-modified vanadium-free titanium alloys. *Electrochim. Acta* **48,** 1395 (2003).
21. C. Morant, M.F. López, A. Gutiérrez, and J.A. Jiménez: AFM and SEM characterization of non-toxic vanadium-free Ti alloys used as biomaterials. *Appl. Surf. Sci.* **220,** 79 (2003).
22. M.F. López, J.A. Jiménez, and A. Gutiérrez: In vitro corrosion behavior of titanium alloys without vanadium. *Electrochim. Acta* **47,** 1359 (2002).
23. A. Gutiérrez, C. Munuera, M.F. López, J.A. Jiménez, C. Morant, T. Matzelle, N. Kruse, and C. Ocal: Surface microstructure of the oxide protective layers grown on vanadium-free Ti alloys for use in biomedical applications. *Surf. Sci.* **600,** 3780 (2006).
24. C. Munuera, T.R. Matzelle, N. Kruse, M.F. López, A. Gutiérrez, J.A. Jiménez, and C. Ocal: Surface elastic properties of Ti alloys modified for medical implants: A force spectroscopy study. *Acta Biomater.* **3,** 113 (2007).
25. M.F. López, J.A. Jiménez, and A. Gutiérrez: Surface characterization of new non-toxic titanium alloys for use as biomaterials. *Surf. Sci.* **482,** 300 (2001).
26. M.F. López, L. Soriano, F.J. Palomares, M. Sánchez-Agudo, G.G. Fuentes, A. Gutiérrez, and J.A. Jiménez: Soft x-ray absorption spectroscopy study of oxide layers on titanium alloys. *Surf. Interface Anal.* **33,** 570 (2002).
27. A. Gutiérrez, M.F. López, J.A. Jiménez, C. Morant, F. Paszti, and A.A. Climent: Surface characterization of the oxide layer grown on Ti–Nb–Zr and Ti–Nb–Al alloys. *Surf. Interface Anal.* **36,** 977 (2004).
28. M. Textor, C. Sittig, V. Frauchiger, S. Tosatti, and D.M. Brunette: Properties and biological significance of natural oxide films on titanium and its alloys, in *Titanium in Medicine*, edited by D.M. Brunette, P. Tengvall, M. Textor, and P. Thomsen (Springer-Verlag, Berlin, Germany, 2001), pp. 171–230.
29. C. Treves, M. Martinesi, M. Stio, A. Gutiérrez, J.A. Jiménez, and M.F. López: Biocompatibility characterization of surface-modified titanium alloys. (unpublished).
30. A. Climent-Font, F. Pászti, G. García, M.T. Fernández-Jiménez, and F. Agulló: First measurements with the Madrid 5 MV tandem accelerator. *Nucl. Instrum. Methods B* **219–220,** 400 (2004).
31. E. Kótai: Computer methods for analysis and simulation of RBS and ERDA spectra. *Nucl. Instrum. Methods B* **85,** 588 (1994).
32. D.B. Lee and S.W. Woo: High temperature oxidation of Ti–47% Al–1.7% W-3.7% Zr alloys. *Intermetallics* **13,** 169 (2005).
33. H.L. Du, P.K. Datta, D.B. Lewis, and J.S. Burnell-Gray: Air oxidation behavior of Ti–6Al–4V alloy between 650 °C and 850 °C. *Corros. Sci.* **36,** 631 (1994).
34. I. Gurappa: Effect of aluminizing on the oxidation behavior of the titanium alloy, IMI 834. *Oxid. Met.* **56,** 73 (2001).
35. L. Gauer, S. Alpèrine, P. Steinmetz, and A. Vassel: Influence of niobium additions on high-temperature-oxidation behavior of Ti_3Al alloys and coatings. *Oxid. Met.* **42,** 49 (1994).
36. F.D. Richardson: in *Physical Chemistry of Melts in Process Metallurgy* (Academic Press, London, UK, 1974).
37. Y.S. Chen and C.J. Rosa: Oxidation characteristics of Ti–4.37 wt% Ta alloy in the temperature range 1258–1473 K. *Oxid. Met.* **14,** 147 (1980).
38. M. Göbel, J.D. Sunderkötter, D.I. Mircea, H. Jenett, and M.F. Stroosnijder: Study of the high-temperature oxidation behavior of Ti and Ti_4Nb with SNMS using tracers. *Surf. Interface Anal.* **29,** 321 (2000).
39. A. Gutiérrez and J. de Damborenea: High-temperature oxidation behavior of laser-surface-alloyed incoloy-800H with Al. *Oxid. Met.* **47,** 259 (1997).
40. M.F. López, A. Gutiérrez, M.C. García-Alonso, and M.L. Escudero: Surface analysis of a heat-treated, Al-containing, iron-based superalloy. *J. Mater. Res.* **13,** 3411 (1998).